GRANT / HQ.

IN-35697

P37

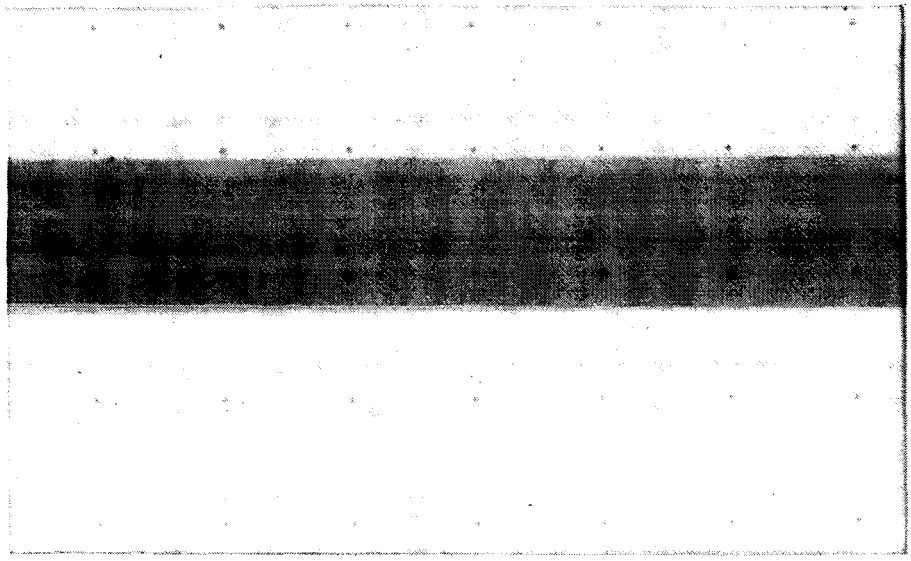

(NASA-CR-179888) THE MARTIAN CLIMATE AND ENERGY BALANCE MODELS WITH CO2/H2O ATMOSPHERES Final Report, 1 Mar. 1984 - 31 Mar. 1986 (New York Univ., New York.) 37 p

N87-11673

Unclas

CSCL 03B G3/91 43931

NEW YORK UNIVERSITY

FACULTY OF ARTS AND SCIENCE

DEPARTMENT OF APPLIED SCIENCE

FINAL REPORT

THE MARTIAN CLIMATE & ENERGY BALANCE MODELS WITH CO_2/H_2O ATMOSPHERES

Martin I. Hoffert
Principal Investigator
NYU/86-154

NASA GRANT NAGW-573

March 1, 1984 - March 31, 1986

New York University
Washington Square
New York, N.Y. 10003

NEW YORK UNIVERSITY

FACULTY OF ARTS AND SCIENCE

DEPARTMENT OF APPLIED SCIENCE

SEASONAL CYCLES OF CO_2 AND ATMOSPHERIC CIRCULATION ON MARS: AN ENERGY BALANCE APPROACH

by
Martin I. Hoffert, Vijay K. Narayanan and Warren H. Ziegler

ABSTRACT

The analysis begins with a seasonal energy balance model (EBM) for Mars. This is used to compute surface temperature versus x = sin(latitude) and time over the seasonal cycle. The core model also computes the evolving boundaries of the CO_2 icecaps, net sublimational/condensation rates, and the resulting seasonal pressure wave. Model results are compared with surface temperature and pressure history data at Viking lander sites, indicating fairly good agreement when meridional heat transport is represented by a thermal diffusion coefficient $D \sim 0.015$ W m^{-2} K^{-1}. Condensational wind distributions are also computed.

An analytic model of Martian wind circulation is then proposed, as an extension of the EBM, which incorporates vertical wind profiles containing an x-dependent function evaluated by substitution in the equation defining the diffusion coefficient. This leads to a parameterization of D(x) and of the meridional circulation which recovers the high surface winds predicted by dynamic Mars atmosphere models ($\sim$ 10 m s^{-1}). Peak diffusion coefficients, $D \sim 0.6$ W m^{-2} K^{-1}, are found over strong Hadley zones — some 40 times larger than those of high-latitude baroclinic eddies. When the wind parameterization is used to find streamline patterns over Martian seasons, the resulting picture shows overturning hemispheric Hadley cells crossing the equator during solstices, and attaining peak intensities during the south summer dust storm season, while condensational winds are most important near the polar caps.

INTRODUCTION

Data from Viking Mars orbiters and landers continues to provide a picture of a sister planet marked by profound seasonal variations in surface temperature, volatile gas exchange and occasional dust storms (Tillman, 1985). Some of the more dramatic events of Mars seasonal cycle are evoked in this descripitive passage (Haberle, 1986a):

> Fall has come to the northern hemisphere of Mars. In the mid-latitudes the mean temperature is dropping past - 70 degrees Celsius; at the north pole it has already reached - 123 degrees, cold enough to freeze carbon dioxide, the principal constituent of the thin Martian atmosphere. A cap of dry ice is now forming on the pole. Before winter ends ice will reach the 50th parallel. Meanwhile in the southern hemisphere winter has ended, and carbon dioxide is evaporating at the south pole. Along the edge of the retreating polar cap a sharp temperature contrast between ice and soil warmed by the spring sun is giving rise to strong winds. During the short but hot southern summer, as Mars makes its closest approach to the sun, the winds will lift dust off the surface in great swirling storms. Ultimately dust may envelop the entire planet.

Much of the prior Viking data analysis, as well a current planning of future Mars science missions, is concerned with understanding meteorological seasonal cycles from observations by spacecraft orbiters and landers. Important related questions are whether and how such cycles have varied over Mars geological history, and the role they play in volatile gas exchange.

Models at different complexity levels are instructive in such studies. For example, energy balance models (EBMs) with atmospheric transport neglected, or schematically depicted by thermal diffusion coefficents, have proven useful in understanding surface thermal physics (Leighton and Murray, 1966; Murray and Malin, 1973; Kieffer et al., 1977; Toon et al., 1980; Hoffert et al., 1981; James and North, 1982; James, 1985),

whereas more computer intensive three-dimensional general circulation models (GCMs) were historically used to model seasonal wind patterns. (Pollack et al. 1976, 1981; Haberle et al., 1979). A simplification based on the nearly zonally-symmetric Mars circulation was exploited by Haberle et al. (1982), who used a two-dimensional dynamic circulation model, including dust storm effects; but extensive computations were still required.

In this paper, simplified dynamics is taken a step further. Employing an integral method with assumed vertical atmospheric profiles, only the numerical solution of the insolation-forced, one-dimensional unsteady heat conduction equation is required. This allows circulation patterns for different seasons and orbital parameters to be rapidly assessed.

The analysis begins with an energy balance approach to derive a core numerical model for surface temperature and carbon dioxide evolution over Mars seasonal cycle. Seasonally-varying temperature and pressure wave data from Viking landers are compared with the core model predictions to establish the realism of this part of the model. Next, new parameterizations of thermally driven and condensation winds, and baroclinic eddy transport effects, are developed. A test of our simple circulation model's surface velocity against existing GCM runs at north summer is presented. Finally, our wind model is employed to estimate the circulation streamline patterns over the four seasons on Mars.

SURFACE ENERGY BALANCE

The core seasonal cycle computer model for $T_s(x,t)$, where x is the sine of the latitude and t is the time, is conceptually similar to that of James and North (1982): It is derived from a zonally-averaged energy balance in the spirit of the original Leighton and Murray (1966) model for seasonal volatile evolution on Mars, but includes the effect of

horizontal atmospheric transport on this balance. The core program yields as by-products the time-varying boundaries of north and south CO_2 icecaps and the rates of mass fluxing to and from the atmosphere from phase changes over the seasonal caps. Model parameters adopted here are summarized in Table 1.

The basic energy balance involves four types of zonally-averaged vertical energy flux per unit surface area in a ground/atmosphere column:

$$H_{sto}(x,t) + H_{sub}(x,t) = H_{rad}(x,t) + H_{hor}(x,t), \qquad (1)$$

where $H_{sto}(x,t)$ is an energy sink by column heat storage, $H_{sub}(x,t)$ is an energy sink to sublimation of an underlying CO_2 frost, $H_{rad}(x,t)$ is a net (solar minus longwave) radiant energy source and $H_{hor}(x,t)$ is an energy source from horizontal atmospheric transport.

Thermal Storage and Sublimation Heat Sinks

Heat is stored during the evolving seasonal cycle by the thermal inertia of the atmosphere and land. The atmosphere mixes fast enough relative to seasonal timescales for the entire column heat capacity to come into play. Its heat capacity per unit area is therefore $C_a \approx \overline{\rho}_s c_p \overline{h} \approx 0.16$ MJ m^{-2} K^{-1}, from Table 1 values.

The effective heat capacity of the underlying ground depends on how deeply the seasonal wave penetrates. with ρ_g, c_g, and λ the ground density, specific heat per unit mass, and thermal conductivity, an annual heating wave of circular frequency $\Omega = 2\pi/\tau_p \approx 1.06 \times 10^{-7}$ rad-s^{-1} produces a thermal wave penetrating to depth $d \approx [2\lambda/(\rho_g c_g \Omega)]^{1/2}$. The corresponding ground heat capacity per unit area is (Hoffert and Storch, 1979)

$$C_g \approx \rho_g c_g d = 2\lambda/(\Omega d) = (2/\Omega)^{1/2} I,$$

where $I = (\rho_g c_g \lambda)^{1/2} = (\Omega/2)^{1/2} C_g$ is the ground thermal inertia. Notice that C_g scales with $\Omega^{-1/2}$, whereas I is a property of surface materials only. A typical ground thermal inertia on Mars is (Pollack et al., 1981) $I \approx 300$ J m^{-2} K^{-1} s$^{-1/2}$, corresponding a heat capacity per unit area of $C_g \approx 1.30$ MJ m^{-2} K^{-1} for the seasonal wave.

The total energy sink from column heat storage is therefore

$$H_{sto}(x,t) \approx C \partial T_s(x,t)/\partial t, \qquad (2)$$

where $C = C_a + C_g \approx 1.46$ MJ m^{-2} K^{-1} is the heat capacity per unit area of the atmosphere plus the thermally interactive ground column.

A unique feature of Mars surface physics over solid CO_2 icecaps is sublimation to the gas phase of the main atmospheric constituent when $T_s > T_c(p_s)$. Conversely, the atmosphere condenses to form CO_2 icecaps when $T_s < T_c(p_s)$. The pressure-dependence of the frost point temperature is approximately $T_c(p_s) \approx -\Theta_L/\ln(p_s/p^*)$, where $p^* \approx 9.74 \times 10^{11}$ Pa is a pressure scale, and $\Theta_L \approx 3148$ K is a temperature scale characterizing the latent heat of sublimation: $L = R\Theta_L \approx 5.95 \times 10^5$ J kg^{-1} (James and North, 1982). Because of the weak logarithmic dependence, as surface pressure p_s varies seasonally over its annual range (600-800 Pa, at the reference ellipsoid elevation), T_c varies over a relatively much smaller range (149-151 K). For simplicity, a constant $T_c \approx 150$ K is assumed over carbon dioxide icecaps. The heat sink to sublimation phase change over CO_2 icecaps is

$$H_{sub}(x,t) = L\dot{m}(x,t). \qquad (3)$$

where $\dot{m}(x,t)$ is the mass per unit time and per unit area injected to (removed from) the atmosphere by phase changes at the surface. This term is nonzero only over CO_2 ice when $T_s \leq T_c$.

Radiation Forcing

Seasonal climate cycles are driven by an insolation function $S(\phi, L_s)$,

where ϕ is the latitude and L_s the heliocentric longitude of the sun — the angular displacement along Mars' elliptic orbit measured from northern hemisphere spring equinox, $L_s \equiv 0$. The eccenticity e, obliquity i and heliocentric longitude of perihelion L_{sp} are parameters of the seasonal cycle, and are available for present epoch from Table 1. The diurnally- averaged incident solar radiation per unit area is given by (Berger, 1978):

$$S(\phi,L_s) \approx \{S_o[1+e\cos(L_s-L_{sp})]^2(H\sin\phi\sin\delta + \cos\phi\cos\delta\sin H)\}/[\pi(1-e^2)^2],$$

where $\delta(L_s)$ is the solar declination angle given by $\sin\delta = \sin i \sin L_s$ and $H(\phi,L_s)$ is the hour angle for sunrise given by $\cos H = -\tan\phi\tan\delta$; Here $H = 0$ and $H = \pi$ correspond to polar night and polar day conditions respectively.

Because Mars accelerates along its orbit near perihelion, and decelerates near apehelion, L_s is nonlinearly related to elapsed time t from some reference point on the orbit. Neglecting terms of order e^2, the time from northern spring equinox is related to L_s approximately by

$$t(L_s) \approx \tau_p/(2\pi)\{L_s - 2e[\sin(L_s - L_{sp}) + \sin L_{sp}]\}.$$

It is also convenient to work with a stretched latitude variable proportional to the area of the planetary surface from the equator,

$$x(\phi) = \sin\phi.$$

These relations define $S(x,t)$ for specified e, i and L_{sp}.

A vertical column containing the atmosphere and thermally interactive ground is heated by a net radiative flux H_{rad} equal to the absorbed

solar flux less the longwave radiation flux lost to space. This term is modeled by

$$H_{rad}(x,t) = S(x,t)(1 - \alpha) - \varepsilon\sigma[T_s(x,t)]^4, \qquad (4)$$

where $\sigma \approx 5.67 \times 10^{-8}$ W m^{-2} K^{-4} is the Stefan-Boltzmann constant and

$$\alpha(x,t) = \begin{pmatrix} \alpha_g \; ; \; T_s(x,t) > T_c \\ \\ \alpha_i \; ; \; T_s(x,t) \leq T_c \end{pmatrix}, \qquad \varepsilon(x,t) = \begin{pmatrix} \varepsilon_g \; ; \; T_s(x,t) > T_c \\ \\ \varepsilon_i \; ; \; T_s(x,t) \leq T_c \end{pmatrix},$$

are planetary albedoes and emissivities, with different values over bare ground and ice. A CO_2 ice albedo of $\alpha_i \approx 0.8$ is assumed over both caps in the program. This is a rough average of north and south cap CO_2 albedos inferred from Viking data by Paige and Ingersoll (1985, Fig. 5). A corresponding ice emissivity of $\varepsilon_i \approx 0.58$ is needed to recover $T_c \approx 150$ K at the poles.

Horizontal Heat Transport

Horizontal (meridional) energy transport arises when winds blow fluid parcels containing enthalpy and gravitational potential energy across latitude circles. The meridional energy flux per unit area is $\rho v(c_p T + gz)$, where ρ, v and T are the density, meridional velocity and temperature; c_p is the constant-pressure specific heat, g the gravitational acceleration and z the altitude. The differential cross-sectional area perpendicular to the meridional energy flux can be written $a(1 - x^2)^{1/2} dz d\lambda$, where λ is the longitude and $x = \sin\phi$. Accordingly, a general, three-dimensional, atmospheric circulation creates an energy flow per unit time across a latitude circle of:

$$F(x,t) = a(1 - x^2)^{1/2} \int_0^{2\pi} \int_0^{\infty} \rho v(c_p T + gz) dz d\lambda. \qquad (5)$$

Since a differential surface area element is $dA_s = 2\pi a^2 dx$, the net energy source per unit surface area into a column of surface area dA_s

from horizontal flows is $H_{hor} = -\partial F/\partial A_s = -(2\pi a^2)^{-1}\partial F/\partial x$; or

$$H_{hor}(x,t) = \frac{\partial}{\partial x}\left[D\,(1-x^2)\,\frac{\partial T_s}{\partial x}\right] \qquad (6)$$

where

$$D(x,t) \equiv \frac{-F(x,t)}{2\pi a^2\,(1-x^2)\partial T_s/\partial x} \qquad (7)$$

is the horizontal diffusivity coefficient for meridional energy flux.

A constant $D \sim 0.015$ w m^{-2} K^{-1} independent of season or latitude was assumed in our initial numerical calculations. As discussed below, this value gave reasonably realistic surface temperatures and seasonal pressure wave distributions in comparison with Viking lander data. However, equations (5) and (7) are crucial links between any known circulation field and the thermal diffusivity. They will be employed subsequently to parametrize D(x) in terms of Mars wind circulation fields.

Numerical Solution

At constant D, substituting equations (2), (3), (4) and (6) into equation (1) gives an unsteady "heat conduction on a sphere" partial differential equation:

$$\frac{\partial T_s}{\partial t} = \frac{1}{\tau}\cdot\frac{\partial}{\partial x}\left[(1-x^2)\frac{\partial T_s}{\partial x}\right] + \frac{S(x,t)(1-\alpha) - \varepsilon\sigma[T_s(x,t)]^4}{C} - \frac{L\dot{m}(x,t)}{C} \qquad (8)$$

where $\tau \equiv C/D \sim 1.0 \times 10^8$ s $\sim 1.6\tau_p$ is a timescale for horizontal diffusive heat transport. Numerical values are for $D \sim 0.015$ W m^{-2} K^{-1}.

Equation (8) is solved numerically for $T_s(x,t)$ by a Crank-Nicholson finite-difference scheme with $\partial T_s/\partial x$ and $\partial^2 T_s/\partial x^2$ approximated by centered differences at interior points, and one-side differences at the poles, where all space derivatives are evaluated at mid-timestep. The implicit Crank-Nicholson PDE solver employs computationally economical tri-diagonal matrices, is unconditionally stable, and has a second-order in space accuracy depending on $\beta = \Delta t/(\tau \Delta x^2)$ (Ferziger, 1981, p. 148). Normally, we want $\beta \leq 1$, corresponding to timesteps $\Delta t < (\tau \Delta x^2)$; that is, the number of timesteps per Mars year needed for a given level of accuracy increases with the square of the horizontal resolution. we use a grid of 40 points in $x = \sin\phi$ ($\Delta x = 0.05$) as a compromise between small Δx desired to resolve icecap boundaries, and large Δx desired to minimize timesteps/year, and thus computing time, at given accuracy. To insure accuracy 1000 steps/year ($\Delta t = 1 \times 10^{-3} \tau_p$) are used corresponding to $\beta \sim 0.2$. A D-coefficient 50 times larger would give $\beta \sim 10$. Some 10,000 steps/year at the same Δx are would be necessary to get $\beta \sim 1$ for an accurate solution.

The program is initialized with a uniform annual mean temperature distribution and "spun up" for several Mars years to eliminate starting transients. It employs the following procedure to compute icecap boundaries and mass fluxes from sublimation/condensation over the caps: Normally $\hbar m = 0$ in equation (6) whenever the computed $T_s(x,t) > T_c$. when the computed surface temperature droped below the frost point, the program sets $T_s(x,t) = T_c$. The time-dependent cap boundaries $x_N(t)$ and $x_S(t)$ are evaluated as the gridpoints in the northern and southern hemisphere, respectively, where equation (7) predicts $T_s = T_c$. Since space and time derivatives of temperature are small over the constant-temperature caps, the sublimation mass source is simply:

$$\dot{m}(x,t) \approx \{S(x,t)(1 - \alpha_i) - \varepsilon_i \sigma T_c^4\}/L. \qquad (9)$$

Balancing net radiant energy against phase change energy is an approximation dating back to the Leighton and Murray (1966) model. It

does seem justified however in light of detailed studies of Mars CO_2 cap energy budgets by Paige and Ingersoll (1985), who found small contributions by transport and storage. Rates of mass injection to the atmosphere by south and north cap sublimation are computed by integrating the mass fluxes per unit area over the respective cap areas,

$$\dot{M}_S(t) = 2\pi a^2 \int_{-1}^{x_S(t)} \dot{m}(x,t)dx, \qquad \dot{M}_N(t) = 2\pi a^2 \int_{x_N(t)}^{+1} \dot{m}(x,t)dx, \tag{10}$$

where negative values indicate mass removal by condensation.

SEASONAL MODEL RESULTS AND VIKING DATA

Figure 1 shows the seasonal variation of pole-to-pole surface temperature computed from the energy balance model for Table 1 parameter values. The results are expressed as constant surface temperature contours at $\Delta T_S = 5$ K intervals on the (x, L_S) plane. Also shown is latitude as a nonlinear vertical scale, $\phi = \phi(x)$, and time in sols from N. Spring equinox as a nonlinear horizontal scale, $t = t(L_S)$.

The hemispheric asymmetry over the seasonal cycle is a consequence of maximum orbital distance from the sun (apehelion) and minimum orbital distance (perihelion) occuring presently at $L_S \approx 70^o$ and 250^o, respectively. These are sufficently close to the southern winter and summer solstices to markedly reenforce the seasonal thermal contrast in the southern hemisphere and diminish it in the northern hemisphere.

The coldest spots on the planet are the CO_2 icecaps at $\approx$ 150 K; the warmest is the southern hemisphere hot spot at $\approx$ 240 K, extending as far south as $\phi \approx 50\ ^oS$ during southern spring and summer. Figure 1 shows the computed seasonal boundaries of the north and south carbon dioxide icecaps $x_N(t)$ and $x_S(t)$, assumed to form at the sublimation frost point temperature, $T_c \approx 150$ K (The "wiggles" in the

receeding cap boundaries are artifacts of the finite Δx resolution of the model). The CO_2 caps are asymmetric with the southern cap extending more equatorward than the north during their respective winter maximums.

The model predictions of seasonal temperature histories at the appropriate latitudes can be directly compared with observations of surface air temperature made by VL-1 and VL-2 landers during the Viking mission. The latitudes of VL-1 (22 ^{o}N — now the Thomas Mutch Memorial Station) and VL-2 (48 ^{o}N) are indicated in Figure 1. Viking lander barometric pressure data at these sites exhibits the well-known seasonal CO_2 pressure waves associated with icecap cycles. The existence of condensation/sublimation pressure waves on Mars was predicted a decade before Viking by Leighton and Murray (1966), who assumed an energy balance model with no atmospheric transport.

Lander Temperatures

Figure 2 compares Mars surface temperatures measured at VL-1 and VL-2 over the seasonal cycle (Seiff, 1982) with predictions of the present energy balance model at the lander latitudes.

The rapid temperature jumps computed during northern spring and summer near the VL-2 site are generated by abrupt sublimations of the receeding north CO_2 polar cap over one spatial step ($\Delta x \approx 0.05$), which propagate south by atmospheric diffusion (Cf. Figure 1). These appear to be artifacts of the finite-difference resolution, and converge to a smooth curve as $\Delta x \rightarrow 0$. With this minor exception, the agreement between the model and the lander observations in both phase and amplitude for the seasonal thermal waves is remarkably good at both sites.

Lander Pressures

A more formidable challenge to the model is its ability to reproduce

the condensation/sublimation seasonal pressure wave observed by the Viking landers. Tillman (1985) has observed that interannual variations in the pressure wave at a given lander location are small. However, even after filtering out short-period oscillations associated with baroclinic "weather" disturbances, the VL-2 pressure wave of any given year is systematically higher than that at VL-1 (Seiff, 1982). This is mainly due to topographic differences at the two sites (VL-1 and VL-2 are at elevations $z_1 = -1.5$ km and $z_2 = -2.5$ km, respectively, relative to the Mars reference ellipsoid).

We therefore corrected the lander pressures $p_j(t)$ in Seiff (1982) to Mars' reference ellipsoid elevation by using the hydrostatic equation: $p_{sj}(t) \approx p_j(t)\exp[+z_j/h_j(t)]$, where $j = 1, 2$. The effects of variations in scale height $h_j(t) = RT_{sj}(t)/g$ from different surface temperature histories $T_{sj}(t)$ at the two sites were included in the correction. Since the z_j's are negative, surface pressures are lower than lander pressures in both cases, with a larger pressure correction for VL-2 (in a deeper valley). The result, shown in Figure 3, is that the VL-1 and VL-2 pressure curves become virtually indistinguishable when these corrections are made. Also shown as an alternate vertical scale in Figure 3 is the atmospheric column mass loading at the "surface" reference ellipsoid elevation, $m = p_s/g$.

To model the seasonal pressure wave, we assumed mass added by phase changes over both caps from equations (10) is deposited in the atmosphere between the cap boundaries. Pressures over the caps are assumed to be maintained constant at the condensation frost point temperature T_c. The rate of change of atmospheric mass between the caps is then

$$\dot{M}_T(t) \equiv 2\pi a^2(x_N - x_S)\frac{\partial}{\partial t}\int_0^{\infty} \rho\, dz = \dot{M}_N(t) + \dot{M}_S(t), \qquad (11)$$

independent of x. For the special case where $\dot{M}_N = -\dot{M}_S$ the net flux into the system is zero; otherwise there is an increase or decrease of atmospheric mass. The surface pressure is assumed to adjust

"instantaneously" planetwide to mass sources, and is found by numerical integration of

$$\frac{dp_s}{dt} = \frac{g\dot{M}_T(t)}{(2\pi a^2)[x_N(t) - x_S(t)]} \qquad (12)$$

The results of this calculation are shown in Figure 3, where they can be directly compared with the lander-observed pressure wave corrected to the reference surface elevation. The pressure peaks result from more rapid degassing by the subliming pole than gas absorption by the condensing pole. The stronger peak in southern summer a consequence of hemispherically asymmetric heating augmented by atmospheric transport. Indeed, a feature supporting the adopted $D \sim 0.015$ W m^{-2} K^{-1}, at least at high latitudes, is its recovery of the observed higher amplitude south summer pressure peak.

James and North (1982) did not obtain the observed relative amplitudes of the seasonal pressure peaks with their "clear sky" diffususion coefficient $D \sim 0.004$ w m^{-2} K^{-1}, although acceptable agreement was found when diffusivity was increased in their model to values as high as $D \sim 0.1$ W m^{-2} K^{-1} during 1977 global dust storms. Their inference is that D correlates with atmospheric opacity, increasing by orders of magnitude during large optical depth global dust storms. Such storms occurred in south summer of the first Viking year (Figure 2), precisely when high atmospheric heat transport is needed to rapidly sublime the south cap. But their correlation with optical depth may be fortuitous, since subsequent years when global dust storms did not recur exhibit essentially the same relative winter and summer peaks in the pressure wave (Tillman, 1985). By chosing a constant $D \sim 0.015$ W m^{-2} K^{-1} — between James and North's "clear sky" and "optically thick" values — we get a fairly realistic pressure curve without invoking the dust storm connection. Even better agreement with the data, based on tuning the relevant paramers within observational constraints, seems possible, but was not pursued.

While the surface temperature curves at Viking lander latitudes are well represented, they may be too insensitive to transport effects to calibrate D. The seasonal pressure wave on the other hand seems mainly influenced by heat transport in the immediate vicinity of the cap boundaries. Clearly, it would be illuminating to if the thermal diffusion coefficient over the planet as a whole could be modeled in terms of dynamic atmospheric processes. This is the subject of the balance of this paper.

MERIDIONAL CIRCULATION

Unlike the earth's atmosphere for which extensive observational statistics on wind patterns are available (Oort, 1983), Mars atmospheric circulation is presently understood primarily from a few GCM simulations over restricted L_S ranges. Existing lander anemometer measurements (Tillman, 1985), surface wind streak patterns (Kahn, 1983), and dust storm observations (Haberle, 1986b) provide only tantalizing hints of the realism of these simulations. At this point therefore, simplified, partly analytical, models are useful tools for gaining insight into atmospheric circulation processes.

Mean and Eddy Flows

A reasonably good approximation is that the time for the atmosphere to radiatively equilibrate with the seasonally evolving surface temperature is sufficient short — about 10 sols according to Pollack *et al.* (1981) — such that the circulation during the seasonal cycle of duration 670 sols is quasi-steady. The time, t, is then a parameter, so time-dependences of flow variables are omitted below for simplicity.

It is also useful to distinguish between zonally-symmetric components of the circulation; and those which vary explicitly with the longitude, λ. Any flow variable can be decomposed into such zonally-symmetric and longitudinally-varying components. Velocity and temperature, for

example, can be written: $v(x,z) + v'(x,z,\lambda)$ and $T(x,z) + T'(x,z,\lambda)$, where primes are departures from the zonal mean. Zonal averages around latitude circles of v' and T' individually vanish identically; but the v'T' product average (the meridional eddy flux) does not. On Mars, it is useful to further decompose $v(x,z)$ into components from condensational winds, and thermally-driven cellular overturning in the meridional plane,

$$v(x,z) = v_c(x) + v_T(x,z). \tag{13}$$

For simplicity, a vertically uniform distribution of condensational wind $v_c(x)$ is assumed. The thermally-driven component $v_T(x,z)$, reverses direction at higher altitudes forming closed Hadley-like cells, and is therefore altitude-dependent. It has the property $\int \rho v_T dz = 0$. Both components transport energy across latitude circles, but only the condensational wind transports mass.

Let meridional diffusion effects from zonally-symmetric processes be represented by a mean-flow diffusion coefficient D_m, those from eddies or waves in the east-west direction by an eddy diffusivity D_e. (Logically, D_m too can be considered an "eddy diffusivity" associated with the mean flow overturning eddies of the Hadley circulation in the x,z plane, but no confusion should result if the terms are understood.) It follows from equations (5) and (7) that the diffusion coefficient is expressible

$$D(x) = D_m(x) + D_e(x), \tag{14}$$

where

$$D_m(x) \equiv \frac{-\int_0^\infty \rho v(c_p T + gz)dz}{a(1-x^2)^{1/2}\,\partial T_s/\partial x}, \tag{15a}$$

$$D_e(x)) \equiv \frac{-\int_0^{2\pi}\int_0^{\infty} \rho c_p [v'T'] dz d\lambda}{2\pi a (1-x^2)^{1/2}\, \partial T_s/\partial x}. \qquad (15b)$$

The eddy component from unstable baroclinic waves can be estimated from Stone's (1972) baroclinic instability parameterization. Its value for the planet as a whole is approximately (Hoffert et al., 1980)

$$D_e \sim \frac{0.28 R^2 p_s c_p \overline{T}_s^{1/2} (\Gamma_{ad} - \overline{\Gamma})^{1/2} (\overline{T}_s - T_c)}{\pi g^{3/2} a^3 f^2} \sim 0.018 \text{ W m}^{-2} \text{ K}^{-1},$$

where the numerical estimate corresponds to Table 1 parameter values and a Coriolis parameter $f \approx 1.4 \times 10^{-4}$ s^{-1}. It is close to the diffusion coefficient value used in the core model ($D \sim 0.015$ W m^{-2} K^{-1}), and may characteristizes transport near the cap boundaries where baroclinic activity dominates (Haberle, 1986b). This may be why the seasonal pressure wave was modeled fairly well.

In contrast to the terrestrial circulation, Martian winds are apparently dominated at low latitudes by the zonally-symmetric circulation (Haberle et al., 1982). We focus next on these components of the circulation, for which no dynamically-linked diffusion parametrization has been developed as yet.

Condensational wind

The mass flowing across a latitude circle carried by the condensational wind is:

$$\dot{M}_c(x) = 2\pi a (1-x^2)^{1/2} \int_0^{\infty} \rho v_c dz. \qquad (16)$$

This quantity appears in the unsteady continuity equation integrated from the surface to the top of the atmosphere:

$$\frac{\partial}{\partial t}\int_0^\infty \rho\, dz \;+\; \frac{1}{a}\frac{\partial}{\partial x}\left[(1-x^2)^{1/2}\int_0^\infty \rho v_c\, dz\right] = 0. \qquad (17)$$

Substituting equations (11) and (16) into (17) yields an expression for the x-wise derivative of the condensational flow, $\partial \dot{M}_c/\partial x = \dot{M}_T/(x_S - x_N)$. We therefore use the linear distribution,

$$\dot{M}_c(x) = (\dot{M}_N + \dot{M}_S)\left(\frac{x - x_N}{x_S - x_N}\right) - \dot{M}_N \qquad (18)$$

which has the proper derivative, and satisfies the cap boundary conditions $\dot{M}_c(x_N) = -\dot{M}_N$ and $\dot{M}_c(x_S) = \dot{M}_S$.

The condensational velocity distribution is obtained by integrating equation (16) with the density profile $\rho(z) \approx \rho_s e^{-z/h}$, where $h = p_s/\rho_s g$ is the scale height:

$$v_c(x) = \frac{g\dot{M}_c(x)}{2\pi a p_s (1-x^2)^{1/2}}. \qquad (19)$$

Condensational winds versus latitude at the equinoxes and solstices computed from equations (18) and (19) using the sources $\dot{M}_N$ and $\dot{M}_S$ from the core program are illustrated in Figure 4. The peak condensational wind magnitude, $v_c \sim 0.4$ m s^{-1}, occurs near the south cap boundary in northern winter ($L_S = 270^o$) as this cap sublimes under the influence of high southern hemisphere insolation and heat transfer to the cap boundary. This wind is comparable in magnitude and location to peak values computed by James (1985, Fig. 3). At this L_S, the condensational flow is everywhere northward, depositing mass in the atmosphere along the way, and contributing to the northern winter peak of Fig. 3, until what remains condenses at the north polar cap. An opposite but weaker flow exists in northern summer ($L_S = 90^o$), when southward flow generated by north cap sublimation is absorbed by the

south cap. If sublimation and condensation rates were precisely equal at opposing caps, condensational winds would still blow, but seasonal pressure waves from this effect would be absent. These winds are weaker at the equinoxes, as expected, but at $L_s = 180^o$, v_c reverses direction mid-planet to accomadate the model prediction of condensation at both caps during this time.

The fact that average condensational winds are of order $v_c \sim 0.2$ m s^{-1} raises an interesting question. The transit time for a gas parcel sublimed at one pole to cross the planet to is $\pi a/vc \sim 5.3 \times 10^7$ s $\sim$ 600 sols, so the time to physically transport condensational mass between VL-1 and VL-2 lander locations is [(48-22)/180] x 600 sols $\sim$ 87 sols. Why then is there no phase lag of this order in the pressure waves observed the two stations? Recall that both lander pressure curves, corrected to the reference ellipsoid and with baroclinic weather oscillations removed, are nearly coincident. One possibility is that the atmosphere rapidly adjusts on the diurnal timescale of internal gravity waves to create horizontally uniform surface pressures. The observational absense of a discernable phase lag seems in any event a sufficient rationale for the instantaneous pressure adjustment assumed in equation (12).

Thermally-driven winds

The zonally-symmetric thermally-driven circulation is composed of a mean merdional circulation, in which the merdional v(x,z) and vertical w(x,z) velocities are coupled by continuity, and a zonal mean wind u(x,z) and temperature T(x,z), which are coupled through the thermal wind relation. These components are in turn coupled through the Coriolis torque. Advection of relative angular momentum in inviscid models is also necessary to describe thermal forcing of the mean meridional circulation.

For nearly inviscid models, the Hadley cell is limited in its latitudinal domain, which in turn limits the intensity of the zonal flow. A major

difference between terrestrial and Martian zonal mean flows is the the relative absense of eddy momentum fluxes on Mars, which makes the circulation nearly zonally symmetric over ± 30° latitudes (Leovy et al., 1973). For example, a two-dimensional zonally symmetric circulation model, such as that employed by Haberle et al., 1982) to study Mars dust storms, would probably not describe the earth's atmospheric circulation very well. As a consequence of the earth's land-sea contrasts eddy momentum fluxes are important at all latitudes, and need to be specified from observations in zonally-averaged models to recover a realistic circulation (MacCracken and Ghan, 1986).

To model D_m an integral method was used in which a meridional wind shear of the form $\partial v/\partial z \approx - \hat{v}(x)/h$ is assumed. This is formally analogous to the zonal wind shear of the thermal wind equation, $\partial u/\partial z \approx \hat{u}(x)/h$, where $\hat{u}(x) = (gh/afT_s)\partial T_s/\partial \phi$ (Washington and Parkinson, 1986). At this point $\hat{v}(x)$ is an unknown function to be determined in terms of $D_m(x)$. However, it is well-known that latitudinal heating gradients drive the zonally-symmetric (u,v) circulation in general (Holton, 1979; Haberle, 1986b). In particular, it follows from equation (15) of Leovy et al. (1973) that for steady, inviscid flows in equatorial regions, and neglecting eddy momentum fluxes, $\hat{v}(x) \sim - \hat{u}(x)$. We therefore assume as a crude approximation that

$$\hat{v}(x) \sim - (gh/afT_s)(1 - x^2)^{1/2}\partial T_s/\partial x \qquad (20)$$

in latitude bands of the Hadley circulation.

The linear profile $v_T(x,z) = - \hat{v}(x)[1 - (z/h)]$ also satisfies zero mass flux across latitude circles, $\int \rho v_T dz = 0$ for $\rho \approx \rho_s e^{-z/h}$, and produces a thermally driven surface wind flowing toward local hot spots ($v_s = v_T(x,0) \propto \partial T_s/\partial x$). This wind reverses direction above the scale height corresponding to overturning Hadley cells, but needs to be carefully interpreted at high altitudes where unrealistically large negative velocities are implied as $z \rightarrow \infty$. The linear profile seems a reasonable

first approximation in the lower troposphere ($z < z_T$), where Mars' "tropopause" is at $z_T \approx 40$ km. The temperature at z_T is $T_T \approx 160$ K.

The scale height is expressible in either of the alternate forms

$$h(x) \approx \frac{RT_s(x)}{g} = \frac{p_s}{\rho_s(x)g}, \tag{21}$$

where typical planetary mean value is $\overline{h} \approx 11$ km. The troposphere lapse rate assuming linear temperature profiles is

$$\Gamma(x) \equiv -\frac{\partial T}{\partial z} \approx \frac{T_s(x) - T_T}{z_T}. \tag{22}$$

The planetary mean lapse rate in Mars' stable atmosphere is $\overline{\Gamma} \approx 1.45 \times 10^{-3}$ K m^{-1}; whereas the adiabatic lapse rate is $\Gamma_{ad} = g/c_p \approx 4.55 \times 10^{-3}$ K m$^{-1} > \Gamma(x)$. It is useful to define a dimensionless relative stability parameter,

$$\gamma(x) \equiv (R/g)[\Gamma_{ad} - \Gamma(x)] \tag{23}$$

To summarize, the vertical structure of the atmosphere is approximated by the profiles,

$$\rho(x,z) \approx \rho_s(x)\exp\{-z/h(x)\}, \tag{24}$$

$$T(x,z) \approx T_0(x) - \Gamma(x)z, \tag{25}$$

$$v(x,z) \approx v_c(x) - \hat{v}(x)\{1 - [z/h(x)]\}. \tag{26}$$

Substituting equations (21)-(26) into equation (15a) and performing the required integrations yields:

$$\hat{v}(x) = -\left\{\frac{ga(1-x^2)^{1/2}\partial T_s/\partial x}{p_s c_p T_s(x)\gamma(x)}\right\} \cdot D_m(x) - \frac{v_c(x)\{1+\gamma(x)\}}{\gamma(x)} \cdot \tag{27}$$

We have departed in equation (27) from the Leovy et al. (1973) integral method in two ways: (i) $\hat{v}(x)$ is evaluated in terms of $D_m(x)$ as opposed to atmospherically-absorbed radiation and (ii) the condensational wind effect is included.

Neglecting condensational winds, and eliminating $\hat{v}(x)$ between equations (20) and (27) with the help of equation (21), gives the following estimate of the zonally-symmetric thermal diffusion coefficient of Hadley cells:

$$D_m \sim \frac{\overline{\rho}_s c_p g \overline{\gamma}}{f} \cdot (\overline{h}/a)^2 \sim 0.6 \text{ W m}^{-2} \text{K}^{-1},$$

using Table 1 values. This is more than 30 times larger than the baroclinic eddy value, D_e, estimated previously. Of course, we would not expect this to apply beyond the x's bounding central Hadley cells, so a rather strong drop-off to values characterizing the cap region is implied.

Both two and three-dimensional primitive equation general circulation models indicate that during solstice conditions cross-equatorial Hadley cells exist surface winds of order $v_s \sim 10 \text{ m s}^{-1}$ over latitudes within $\pm 30^\circ$ of the equator (Haberle et al., 1982). Typical surface wind distributions, $v_s(x)$, during south summer computed with two-dimensional (2D, Haberle et al., 1982) and three-dimensional (3D, Pollack et al., 1976) dynamic models are shown in Figure 5. These dynamically explicit models are identical mathematically and numerically, except that λ-derivatives are set equal to zero in the 2D model, automatically suppressing any longitudinal waves or eddies. The closeness of the 2D and 3D results supports the assumed dominance of the zonally symmetric winds. These zonal mean meridional surface winds on Mars are substantially more intense than their terrestrial counterparts — the latter being of order $v_s \sim 1 \text{ m s}^{-1}$ (Oort, 1983, p. 157).

We sought to determine whether a $D_m(x)$ distribution could be found with peak values of $D_{max} \sim 0.6$ W m^{-2} K^{-1} which approximates the surface wind distributions of the dynamic models. To test this we used T_s, $\partial T_s/\partial x$, γ and v_c versus x from the core model at $L_s = 90^o$ — close, but not identical, to the GCM $L_s \approx 106^o$ conditions — and evaluated our model's corresponding surface velocity

$$v_s(x) = \left(\frac{ga(1-x^2)^{1/2}\partial T_s/\partial x}{p_s c_p T_s(x)\gamma(x)} \right) \cdot D_m(x) + \frac{v_c(x)\{1 + 2\gamma(x)\}}{\gamma(x)},$$

for various assumed functions $D_m(x)$.

An immediate finding was that surface wind distributions consistent with GCM results at all latitudes could not be obtained with a latitude-independent diffusion coefficient. A constant D_m, matching $v_s \sim 10$ m s^{-1} over Hadley cell regions gave too large surface winds near the cap boundaries (where $\partial T_s/\partial x$ is large), while a small D_m could recover cap region surface winds, but not those of Hadley zones. Clearly, a latitudinally-varying diffusion coefficent is required.

By experimenting with different functions, a reasonably successful diffusion coefficient distribution was found. As shown in Figure 5, the model produced a $v_s(x)$ distribution close to those of the dynamic models — almost as close as the 2D and 3D surface wind distributions are to each other — when the logarithm of D_m varied parabolically with x between the cap boundaries. This was a very welcome finding, as it was not even certain a priori that a diffusivity approximation would appropriately describe the zonally-symmetric circulation. As it happened, we were able to take the results even a further step to compute the streamlines.

In Figure 5 (TOP) the $D_m(x)$ used can be compared with James and North's "clear sky" and "dust storm" diffusion coefficients discussed

previously, and typical values of the baroclinic eddy component D_e. This $D_m(x)$ can be written

$$\ln D_m(x) = \ln D_{min}[1 - 4Kf(x)], \qquad (28)$$

where $K = [(\ln D_{max} / \ln D_{min}) - 1]$ and $f(x) = [(x - x_S)(x - x_N)/(x_N - x_S)^2]$. Diffusivity is a minimum ($D_{min} = 0.015$ W m^{-2} K^{-1}) at the cap boundaries x_N and x_S, and peaks ($D_{max} = 0.60$ W m^{-2} K^{-1}) midway between the cap boundaries. Near cap boundaries, $D_m(x)$ is sufficiently small that surface velocity is dominated by condensational winds, $v_s \sim v_c(1+2\gamma)/\gamma$. For $\gamma \sim 0.15$, and $v_c \sim -0.2$ m s^{-1}, this gives a southward surface velocity near the cap boundaries of $v_s \sim -2$ m s^{-1}, close to values shown of Figure 5. Notice that the surface winds induced by the condensational winds exceed them by almost an order of magnitude, an effect produced in the dynamic models as well.

Despite many approximations, the model reproduces GCM surface wind patterns near north summer solstice suprisingly well, including three overturning cells and condensation wind effects. Even details like the local surface velocity dip near the equator produced by the solar heating function are recovered.

An interesting result was that the diffusion coefficient is much larger across Mars Hadley cells, than at the cap boundaries. A comparable, but latitude-independent $D \sim 0.6$ W m^{-2} K^{-1}, will match observed zonal mean surface temperature distributions on earth (Hoffert et al., 1983) — also surprising in light of the earth's 100 times greater surface pressure. In the terrestrial case, this must result from very different flow mechanisms including atmospheric eddy transport and ocean currents.

Streamlines

In our flow model, equations (19) and (26)-(28) together with information from the core EBM, define the zonally-symmetric

meridional velocity field v(x,z) at any time during the seasonal cycle. These patterns are more clearly visualized by looking at the streamline contours, than at the velocity field as such.

The partly analytic nature of the model makes streamline calculations fairly straightforward: A streamfunction $\Psi(x,z)$ can be defined by its partial derivatives $\partial\Psi/\partial x = -2\pi a^2 \rho w$ and $\partial\Psi/\partial z = 2\pi a(1 - x^2)^{1/2} \rho v$ such that continuity is identically satisfied:

$$\frac{\partial(\rho w)}{\partial z} + \frac{\partial\,[(1-x^2)^{1/2}\rho v]}{a\,\partial x} = 1/(2\pi a^2)\left\{ - \frac{\partial^2\Psi}{\partial z \partial x} + \frac{\partial^2\Psi}{\partial x \partial z} \right\} = 0.$$

The streamlines — contours of constant mass flow per unit time across which there is no flow — are therefore available from

$$\Psi(x,z) = 2\pi a(1 - x^2)^{1/2} \int_0^z \rho(x,z')v(x,z')\,dz'.$$

Substituting equations (24) and (26) and integrating gives:

$$\Psi(x,z) = 2\pi a(1 - x^2)^{1/2}(p_s/g)\{- \hat{v}(x)\cdot[z/h]\cdot e^{-z/h} + v_c(x)\cdot[1 - e^{-z/h}]\}. \quad (29)$$

Notice that the streamfunction at the top of the atmosphere equals the condensation mass flux $\Psi(x, \infty) = \dot{M}_c(x)$, and that the surface and poles are zero mass flux boundaries. $\Psi(x,0) = \Psi(\pm 1, z) = 0$.

Figure 6 shows the meridional plane streamlines computed at $L_s = 0^o$, 90^o, 180^o and 270^o. The contours of constant Ψ have units of Megatonnes per second (1 Mt $s^{-1} = 10^9$ kg s^{-1}), and in the present sign convention are < 0 for clockwise circulations in the x,z plane. At north spring equinox we find north and south Hadley cells of roughly comparable intensity in each hemisphere with core flows centered at the scale height. A weak hemispheric asymmetry is produced even at equinoctal conditions because the ground thermal inertia produces asymmetric surface temperature distributions which "remember" their

history.

As the northern hemisphere warms during its summer solstice, the south main cell migrates northward, penetrating to some 30^{o} N latitude, and intensifies to flow rates of $\sim$ 18 Mts^{-1}; At the same time the northern cell weakens, and a weak indirect cell is produced near the south cap boundary by condensational winds. The Hadley cells become more nearly balanced in the two hemispheres at northern fall equinox, although again there is some hemispheric asymmetry. Finally, during northern winter solstice (southern summer), the northern cell's boundary moves southward, and attains a core circulation of $\sim$ 28 Mt s^{-1} — the highest intensity of the seasonal cycle. Indeed, southern summer is the time of year on Mars when intense surface winds can attain the saltation velocities needed to raise particulate matter into the atmosphere. This is often a precursor of global-scale dust storms.

CONCLUDING REMARKS

We have seen that the core energy balance model developed in the early part of this paper gave a reasonably good account of the seasonal surface temperature and pressure waves on Mars as recorded by the Viking landers. Moreover, our extension to wind field analysis of the energy balance approach gives qualitatively plausible descriptions of atmospheric circulation over all seasons, and inherently recovers GCM-predicted surface winds at the north summer calibration point. The wind field depends partly on the pole-to-pole surface temperature distribution, and partly on the parameterized diffusion coefficient distribution.

More work is needed on modeling the diffusion coefficient distribution in terms of limitations on the boundaries of the Hadley circulation from angular momentum and stability constraints. Moreover, a feedback on the core model is suggested by the wind field analysis: In particular, internally-consistent calculations of surface temperatures at equatorial latitudes should employ the $D_m(x)$ of the wind analysis in

the heat conduction equation, as opposed the the constant D ~ 0.015 W m^{-2} K^{-1} assumed here. In turn, surface temperatures computed with this $D_m(x)$ feed back on the wind field. Prior to our wind analysis, we accepted the conventional wisdom of a largely decoupled lunar-like planet in which atmospheric transport feedbacks on surface temperature distributions are small and confined to polar cap boundaries. This assumption needs to be reexamined.

In light of its computational economy compared to GCMs, applications of the present approach to related phenomena of the Mars seasonal cycle are promising areas of future research. For example, in the Mars seasonal hydrological cycle as modeled by James (1985), it is assumed that meridional transport of water vapor is accomplished by condensational winds plus some unspecified diffusionlike process. Our wind model suggests Hadley Cell transport, in which the small scale height of H_2O profiles would selectively favor transport by near-surface winds, might provide an explicit explanation of this "diffusive" transport. Viking orbiter data on vertically-integrated water vapor are available for testing such models.

Another potential application is modeling of Martian dust storms. The zonally-symmetric circulations simulated by Haberle et al. (1982) at south summer conditions demonstrate that positive radiative feedbacks from dust raised by surface winds strengthens and expands the Hadley circulation. A puzzling question is why global dust storms are not triggered every Mars year. The answer may be related to the interplay of the zonally-symmetric and baroclinic eddy components of the circulation (Haberle, 1986b). Although as presently configured our model does not incorporate the radiative feedbacks needed to mimic such global dust storms, such extensions can be implimented in principle. A simplified representation of zonally symmetric and baroclinic eddy transports, including the influence of vertical thermal structure, might well provide useful insights into the complex dynamics of dust storm events.

Finally, the present approach seems well suited to studies where runs over a large parameter space are needed. These include sensitivity studies, analyses of Mars paleoclimate when orbital parameters were different, and analysis of future scientific missions to Mars — where instrument design may require estimates of meteorological conditions over entire annual cycles.

ACKNOWLEDGEMENTS

We thank Robert Haberle, Phillip James and James Tillman for stimulating discussions of the Mars seasonal cycles. This research was supported by the National Aeronautics and Space Administration, Mars Data Analysis Program, under NASA Grant NAGW-573 to New York University.

REFERENCES

BERGER, A.L. (1978) Long-term variations of daily insolation and quaternary climate changes. J. Atmos. Sci. **35**, 2362-2367.

FERZIGER, J.H. (1981) Numerical Methods for Engineering Application. John wiley and Sons, New York, 270 pp.

HABERLE, R.M. (1986a) The climate of Mars. Scientific American **254** (5), 54-62 (May, 1986).

HABERLE, R.M. (1986b) Interannual variability of global dust storms on Mars. Science **234**, 459-461 (October 24, 1986).

HABERLE, R.M., C.B. LEOVY, AND J.B. POLLACK (1979) A numerical model of the Martian polar cap winds. Icarus **39**, 151-183.

HABERLE, R.M., C.B. LEOVY, AND J.B. POLLACK (1982) Some effects of global dust storms on the atmospheric circulation of Mars. Icarus **50**, 322-367.

HOFFERT, M.I., A.J. CALLEGARI, C.T. HSIEH, AND W. ZIEGLER (1981) Liquid

water on Mars: An energy balance climate model for CO_2/H_2O atmospheres. Icarus 47, 112-129.

HOFFERT, M.I., B.P. FLANNERY, A.J. CALLEGARI, C.T. HSIEH, AND W. WISCOMBE, (1983) Evaporation-limited tropical temperatures as a constraint on climate sensitivity. J. Atmos. Sci. 40, 1659-1668.

HOFFERT, M.I., AND J. STORCH (1979) A scheme for computing surface fluxes from mean flow observations. Boundary-Layer Meteorology 17, 429-442.

HOLTON, J.R. (1979) An Introduction to Dynamic Meteorology (2nd Edition). Academic Press, New York.

JAMES, P.B. (1985) The Martian hydrological cycle: Effects of CO_2 mass flux on global water distribution. Icarus 64, 249-264.

JAMES, P. B., AND G.R. NORTH (1982) The seasonal CO_2 cycle on Mars: An application of an energy balance climate model. J. Geophys. Res. 87, 10,271-10,283.

KAHN, R. (1983) Some observational constraints on the global-scale wind system on Mars. J. Geophys. Res. 88, 10,189-10.209.

KIEFFER, H.H., T.Z. MARTIN, A.R. PETERFREUND, B.M. JAKOSKY, E.D. MINER, AND F.D. PALLUCONI, (1977) Thermal and albedo mapping of Mars during the Viking primary mission. J. Geophys. Res, 82 (28), 4249-4291.

LEIGHTON, R.R., AND B.C. MURRAY (1966) Behavior of carbon dioxide and other volatiles on Mars. Science 153, 136-144.

LEOVY, C.B., R.W. ZUREK, AND J.B. POLLACK (1973) Mechanisms for Mars dust storms. J. Atmos. Sci, 30, 749-762.

MACCRACKEN, M.C. AND S.J. GHAN (1986) Design and use of zonally-averaged climate models. UCRL-94338 Preprint, Lawrence Livermore National Laboratory, Livermore, CA (March, 1986).

MURRAY, B.C., AND M.C. MALIN, (1973) Polar volatiles on Mars — Theory versus observation. Science 182, 437-433.

OORT, A.H. (1983) Global Atmospheric Circulation Statistics, 1958-1973. NOAA Professional Paper 14. U.S. Department of Commerce, National Oceanic and Atmospheric Administration, Rockville, Maryland.

PAIGE, D.A. AND A.P. INGERSOLL, (1985) Annual heat balance of Martian polar caps: Viking observations. Science 228, 1160-1168.

POLLACK, J.B. (1981) Atmospheres of the terrestrial planets. In: BEATTY, J.K., O'LEARY, B. AND CHAIKEN, A. (Eds.) The New Solar System, Cambridge University Press, New York pp. 57-70.

POLLACK, J.B., C.B. LEOVY, Y. MINTZ, AND W. VAN CAMP (1976) Winds on Mars during the Viking season: Predictions based on a general circulation model with topography. Geophys. Res. Lett., 3, 479-482.

POLLACK, J.B., C.B. LEOVY, P.W. GREIMAN, AND Y. MINTZ (1981) A Martian general circulation experiment with large topography. J. Atmos. Sci. 38, 3-29.

SEIFF, A. (1982) Post-Viking models for the structure of the summer atmosphere of Mars. Adv. Space Res, 2, 3-17.

STONE, P.H. (1974) The meridional variation of the eddy heat fluxes by baroclinic waves and their parameterization. J. Atmos. Sci. 31, 444-456.

TILLMAN, J.E. (1985) Martian meteorology and dust storms from Viking observations. In: MCKAY, C. (Ed) The Case for Mars 2. American Astronomical Society, Science and Technology Series, Vol. 65, pp. 333-342.

TOON, O.B., J.B. POLLACK, W. WARD, J.A. BURNS, AND K. BILSKI (1980) The astronomical theory of climate change on Mars. Icarus 44, 552-607.

WASHINGTON, W.M. AND C.L. PARKINSON (1986) An Introduction to Three-Dimensional Climate Modeling. University Science Books, Mill Valley, California.

Table 1. ORBITAL AND PHYSICAL CHARACTERISTICS OF MARS (CURRENT EPOCH)

Property	Value	Units
Annual period, $\tau_p = 2\pi/\Omega$	5.94×10^7	[s]
Diurnal period, τ_d, 1 sol	8.86×10^4	[s]
Eccentricity, e	0.0934	[-]
Obliquity (spin axis tilt), i	25.1	[deg]
heliocentric longtude of perihelion, L_{sp}	250	[deg]
Solar constant, S_o	586	[w m^{-2}]
Planetary radius, a	3.39×10^6	[m]
Gravitational acceleration, g	3.73	[m s^{-2}]
Bare ground heat capacity per unit area, C_g	1.30×10^6	[J m^{-2} K^{-1}]
Bare ground thermal inertia, I	300	[J m^{-2} K^{-1} $s^{-1/2}$]
Bare ground albedo, α_g	0.30	[-]
Bare ground emissivity, ε_g	1.00	[-]
Ice albedo, α_i	0.80	[-]
Ice emissivity, ε_i	0.58	[-]
Ice sublimation temperature, T_c	150	[K]
Latent heat of CO_2 ice sublimation, L	5.95×10^5	[J kg^{-1}]
Gas constant, R	189	[J kg^{-1} K^{-1}]
Atmosphere specific heat, c_p	830	[J kg^{-1} K^{-1}]
Mean surface pressure, $\overline{p}_s$	700	[Pa]
Mean mass per surface area, $\overline{m} = \overline{p}_s/g$	188	[kg m^{-2}]
Mean surface temperature, $\overline{T}_s$	218	[K]
Mean surface density, $\overline{\rho}_s = \overline{p}_s/R\overline{T}_s$	0.0170	[kg m^{-3}]
Mean scale height, $\overline{h} = R\overline{T}_s/g$	1.1×10^4	[m]
Tropopause height, z_T	4.0×10^4	[m]
Tropopause temperature, T_T	160	[K]
Adiabatic lapse rate, $\Gamma_{ad} = g/c_p$	4.55×10^{-3}	[K m^{-1}]
Mean tropospheric lapse rate, $\overline{\Gamma} = (\overline{T}_s - T_T)/z_T$	1.45×10^{-3}	[K m^{-1}]
Mean stability parameter, $\overline{\gamma} = (R/g)(\Gamma_{ad} - \overline{\Gamma})$	0.15	[-]

FIGURE CAPTIONS

Figure 1. Mars seasonal surface isotherms computed from the present model.

Figure 2. Seasonal variation of near-surface atmospheric temperatures at Viking lander sites (Seiff, 1982) compared with present energy balance model predictions.

Figure 3. Seasonal variation of atmospheric pressure (reduced to Mars reference ellipsoid) at Viking lander sites compared with present energy model predictions.

Figure 4. Latitudinal distribution of condensational winds at north spring equinox ($L_S = 0^o$), north summer solstice ($L_S = 90^o$), north fall solstice ($L_S = 180^o$) and north winter solstice ($L_S = 270^o$). Wind directions are positive toward the North Pole.

Figure 5. (TOP). Diffusion coefficient distribution D(x) used to match surface wind distribution of dynamic circulation models; (BOTTOM) Surface velocity distributions near north summer solstice. Present model results are for $D_m = D(x)$ at $L_S = 90^o$.

Figure 6. Streamline patterns on Mars over the four seasons from the present model.

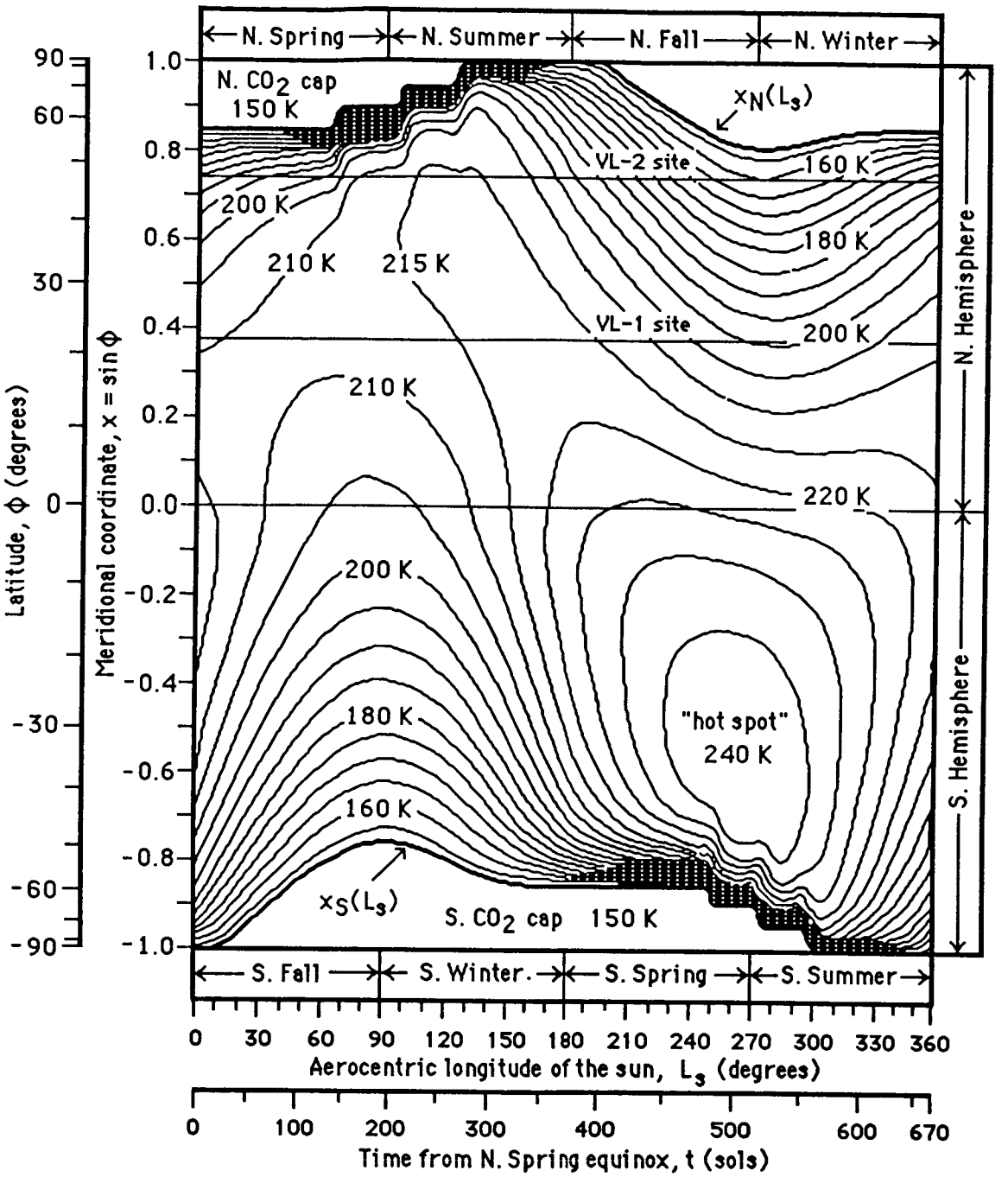
N. Spring
N. Summer
N. Fall
N. Winter
N. CO_2 cap
150 K
$x_N(L_s)$
VL-2 site
160 K
200 K
180 K
210 K
215 K
VL-1 site
200 K
210 K
220 K
200 K
"hot spot"
240 K
180 K
160 K
$x_S(L_s)$
S. CO_2 cap 150 K
S. Fall
S. Winter.
S. Spring
S. Summer
N. Hemisphere
S. Hemisphere
Latitude, φ (degrees)
Meridional coordinate, x = sin φ
90
60
30
0
-30
-60
-90
1.0
0.8
0.6
0.4
0.2
0.0
-0.2
-0.4
-0.6
-0.8
-1.0
0 30 60 90 120 150 180 210 240 270 300 330 360
Aerocentric longitude of the sun, L_s (degrees)
0 100 200 300 400 500 600 670
Time from N. Spring equinox, t (sols)

Figure 1

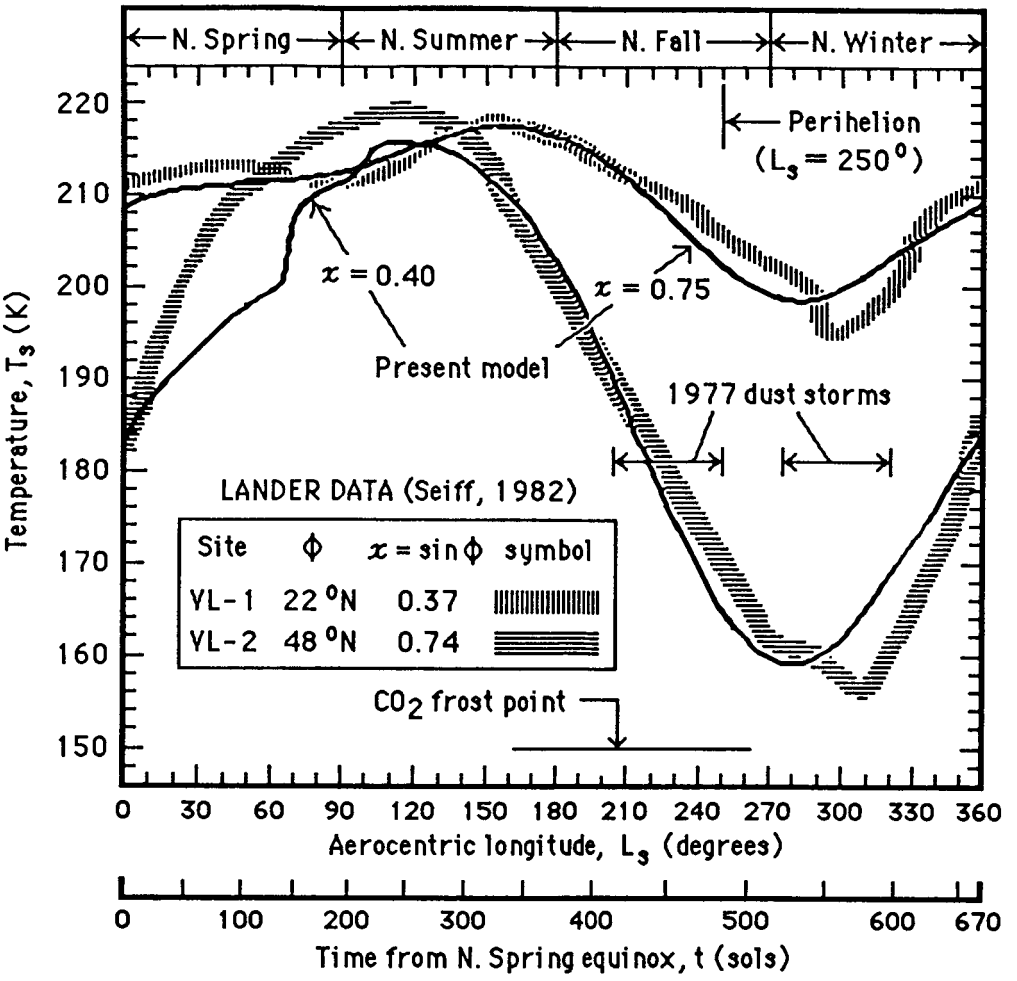
N. Spring
N. Summer
N. Fall
N. Winter
Perihelion
($L_s = 250^0$)
$x = 0.40$
$x = 0.75$
Present model
1977 dust storms
LANDER DATA (Seiff, 1982)
Site ϕ $x = \sin\phi$ symbol
VL-1 22 °N 0.37
VL-2 48 °N 0.74
CO_2 frost point
Temperature, T_s (K)
220
210
200
190
180
170
160
150
0 30 60 90 120 150 180 210 240 270 300 330 360
Aerocentric longitude, L_s (degrees)
0 100 200 300 400 500 600 670
Time from N. Spring equinox, t (sols)

Figure 2

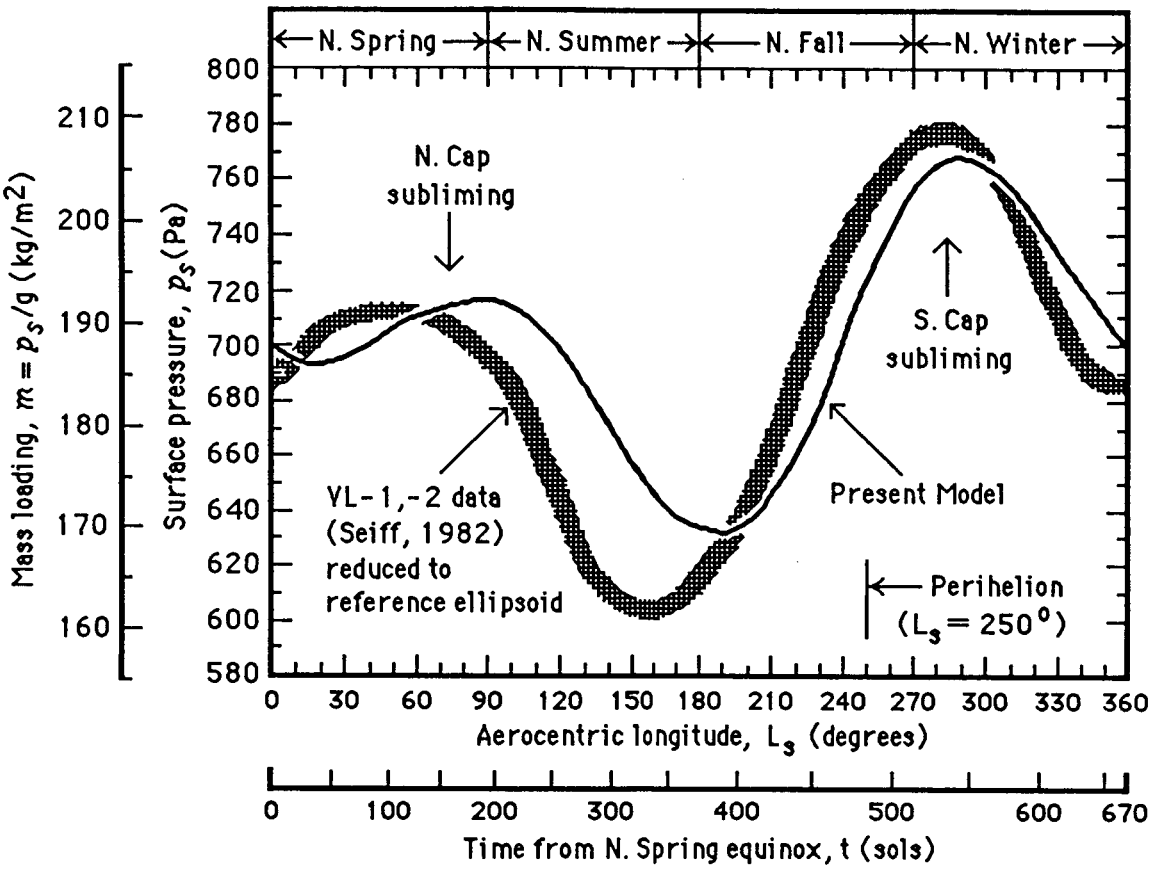
← N. Spring →
← N. Summer →
← N. Fall →
← N. Winter →
N. Cap subliming
S. Cap subliming
VL-1,-2 data (Seiff, 1982) reduced to reference ellipsoid
Present Model
← Perihelion ($L_s = 250^0$)
Mass loading, $m = p_s/g$ (kg/m^2)
Surface pressure, p_s (Pa)
210
200
190
180
170
160
800
780
760
740
720
700
680
660
640
620
600
580
0 30 60 90 120 150 180 210 240 270 300 330 360
Aerocentric longitude, L_s (degrees)
0 100 200 300 400 500 600 670
Time from N. Spring equinox, t (sols)

Figure 3

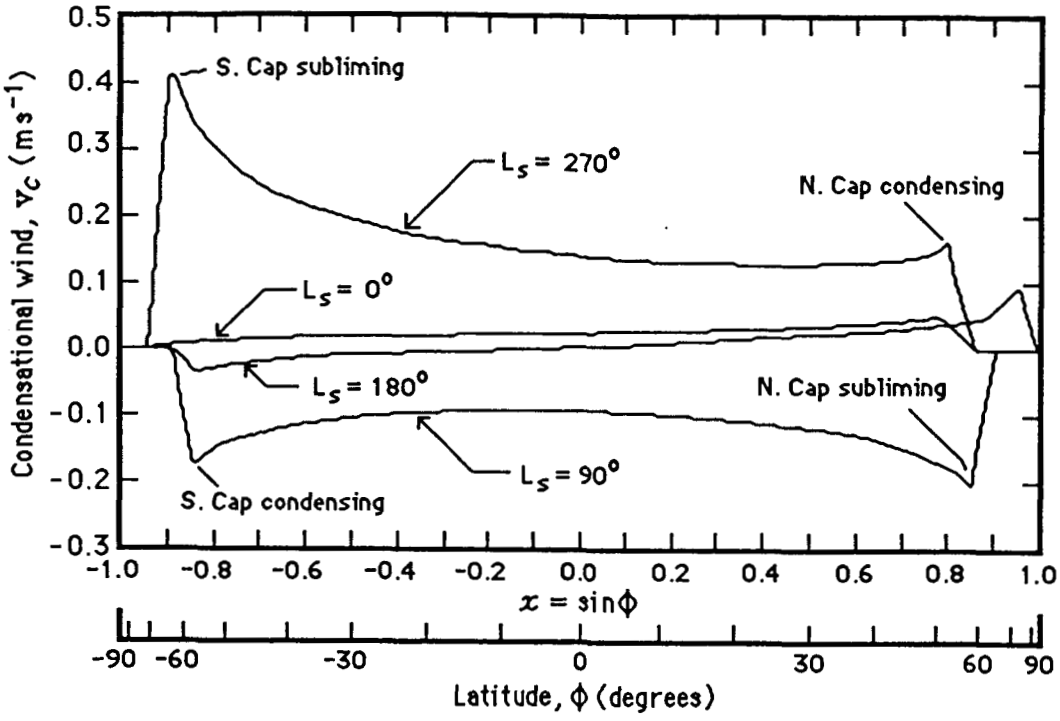
S. Cap subliming
$L_s = 270°$
N. Cap condensing
$L_s = 0°$
$L_s = 180°$
N. Cap subliming
$L_s = 90°$
S. Cap condensing
Condensational wind, v_c (ms^{-1})
0.5
0.4
0.3
0.2
0.1
0.0
-0.1
-0.2
-0.3
-1.0 -0.8 -0.6 -0.4 -0.2 0.0 0.2 0.4 0.6 0.8 1.0
$x = \sin\phi$
-90 -60 -30 0 30 60 90
Latitude, ϕ (degrees)

Figure 4

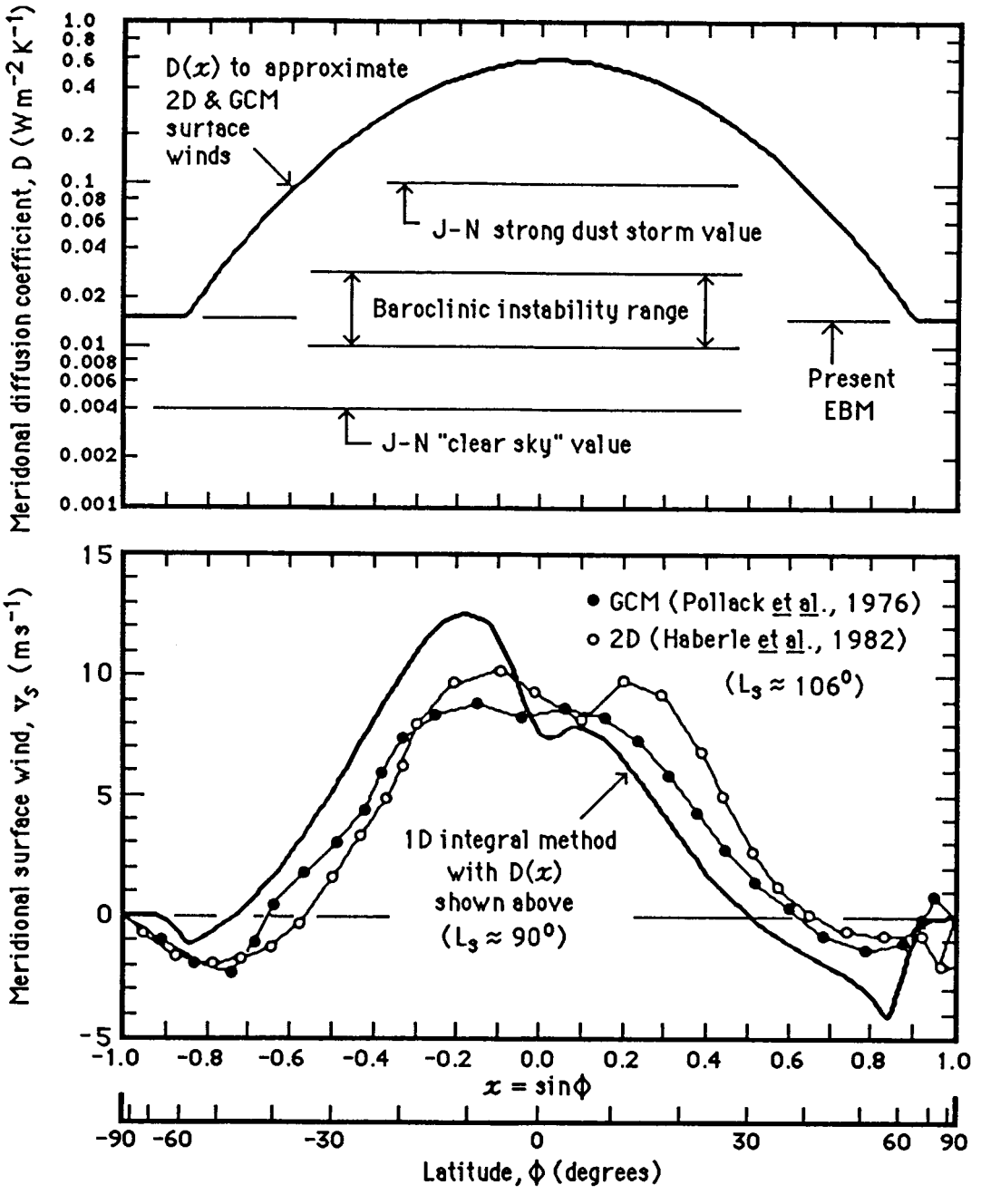
Meridonal diffusion coefficient, D (W m^{-2} K^{-1})
1.0
0.8
0.6
0.4
0.2
0.1
0.08
0.06
0.04
0.02
0.01
0.008
0.006
0.004
0.002
0.001
D(x) to approximate 2D & GCM surface winds
J-N strong dust storm value
Baroclinic instability range
Present EBM
J-N "clear sky" value
Meridional surface wind, v_s (m s^{-1})
15
10
5
0
-5
• GCM (Pollack et al., 1976)
o 2D (Haberle et al., 1982)
($L_s \approx 106^0$)
1D integral method with D(x) shown above
($L_s \approx 90^0$)
-1.0 -0.8 -0.6 -0.4 -0.2 0.0 0.2 0.4 0.6 0.8 1.0
$x = \sin\phi$
-90 -60 -30 0 30 60 90
Latitude, ϕ (degrees)

Figure 5

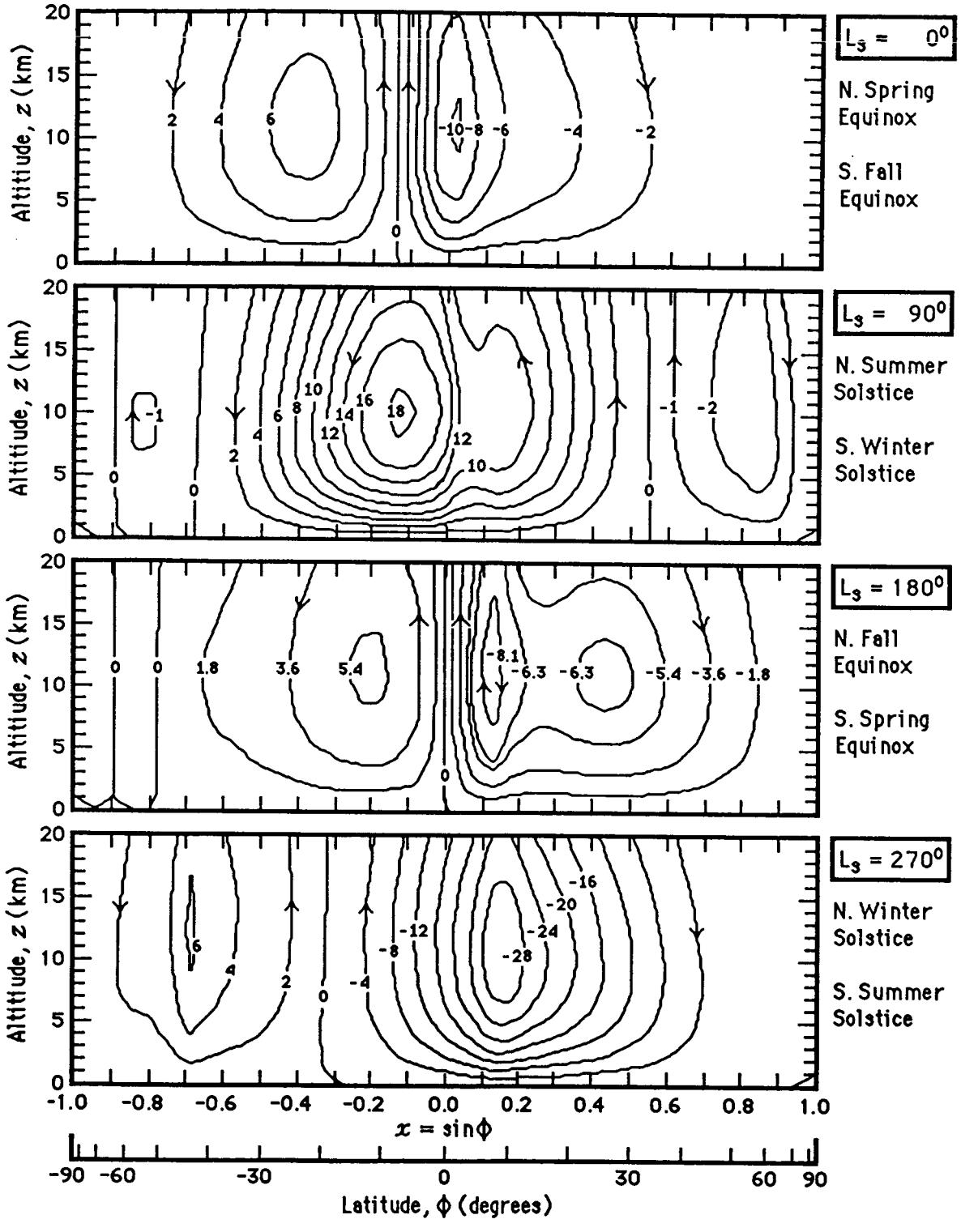
Altitude, z (km)
L_s = 0°
N. Spring Equinox
S. Fall Equinox
L_s = 90°
N. Summer Solstice
S. Winter Solstice
L_s = 180°
N. Fall Equinox
S. Spring Equinox
L_s = 270°
N. Winter Solstice
S. Summer Solstice
$x = \sin\phi$
Latitude, ϕ (degrees)

Figure 6